Swift and NuSTAR observations of XTE J1859+083

Bachelorarbeit aus der Physik

Vorgelegt von:
Jakob Stierhof
30. November 2015

Dr. Karl Remeis Sternwarte Bamberg
Friedrich-Alexander-Universität Erlangen-Nürnberg

Betreuer: Prof. Dr. Jörn Wilms

I report research on the observed outburst early in 2015 of the high mass X-ray binary XTE J1859+083 done with *NuSTAR* and *Swift*/XTE. The overall intention was to apply the spectral model reported from Farinelli et al. (2012). The model reproduces the observed spectrum over the energy range of 2 – 50 keV. Furthermore, I found the rotation period of $9.791507 \pm 8 \cdot 10^{-6}$ s which is in accordance to the period reported by Marshall et al. (1999). Pulse profile analysis reveals nearly no dependency on energy.

The attempt to locate the source from the *NuSTAR* images within a lower error radius showed that the location on the detector modules does not contribute to the uncertainty and only deviations in the pointing direction limit the position estimation within a $3''$ error radius to R.A. $= 18^{\mathrm{h}}\,59^{\mathrm{m}}\,2.2^{\mathrm{s}}$, Dec $= 8^{\circ}\,14'\,43''$ for module A.

Contents

1 Introduction

The topic of this thesis is to investigate the X-ray binary system XTE J1859+083 with performed observations by the *NuSTAR* and *Swift* telescopes. The X-ray source was discovered in 1999 (Marshall et al., 1999) with the *Rossi X-ray Timing Explorer* (RXTE). Since the detection the field around the source got only observed two more times in detail. Corbet et al. (2009) used archival data of *BeppoSAX* Wide Field Camera and RXTE and located the position at R.A. $= 18^h\,59^m\,2.4^s$, Dec. $= +8^\circ\,13'\,57''$ with an error radius of $1'$ (90% confidence) which is consistent with the detection from Marshall et al. (1999). They also suggested a possible modulation due to orbital motion with a period of 60.65 ± 0.08 d which is consistent, together with the 9.801 ± 0.002 s pulsation period reported by Marshall et al. (1999), for XTE J1859+083 to be a Be/neutron star binary system. A newer observation reported by Romano et al. (2007) with *Swift*'s X-ray Telescope for 9.7 ks of the error region showed no significant X-ray source.

The latest outburst of XTE J1859+083 was reported on February 8th 2015 by the MAXI/GSC nova alert system (Negoro et al., 2015) and confirmed by the BAT hard X-ray transient monitor (Krimm et al., 2015). Observations with *Swift* followed right after and the observations of *NuSTAR* and *Swift* used in this thesis were done on March 3rd 2015.

To understand the extreme conditions around neutron stars (NS) it is helpful to take a look at the birth of these compact objects in general. A NS is a remnant at the end of many stars evolution. The conditions under which a NS arise is well examined and described.

The common way to create a NS is when a high mass star ends its life in a Type-II supernova witch a progenitor mass of at least $8\,M_\odot$ (Smartt, 2009). Once a gas cloud collapses under gravitational force and forms a ball of hot plasma, fusing hydrogen to helium in its core, a star is born. The evolution of stars is in detail very complicated and not the topic of this thesis. Nevertheless I will shortly describe how stars in general undergo the main sequence and why and under which conditions they evolve to the different observable remnants.

Stars like the sun have very low mass and the fusion process occures only in the core. Starting with fusing hydrogen to helium the star produces increasingly higher mass elements progressing through the periodic table until the net energy gained from the fusion process is below zero. This is the case when the star starts fusing iron. While producing higher and higher elements the star has to burn with increasing heat. Therefore the pressure inside the star increases as well and forces the star to grow in size. In this process the star ejects the outer parts of its atmosphere remaining only the iron core at the end. Once there and in mass below the Chandrasekhar limit of $1.44\,M_\odot$ the core is no longer in equilibrium between the gravitational force and on temperature base pressure but by the gravitation and pressure due to degenerated electron gas (Pauli principle). The remnant, called "white dwarf", only glows due to thermal energy. Characteristic numbers for white dwarfs are mass $M \approx 1\,M_\odot$ and radius $R \approx 10^{-2}\,R_\odot$.

Only if the mass of the star is greater then the mentioned $8\,M_\odot$ then it will end its former attendance in a bright supernova and left a NS behind. On its way the star fuses simultaneous hydrogen and heavier elements in an onion-like structure (Fig. 1.1). Where elements with higher mass are at the inner shells.

Once the core starts fusing iron the star gains no more energy. This causes the core to shrink and due to the high mass the surrounding shells get strong accelerated inwards. If the core mass is above the Chandrasekhar limit, the star implodes within fractions of seconds. The energy from the outer shells heats the core up to temperatures of 10^{11} K, producing neutrons and neutrinos

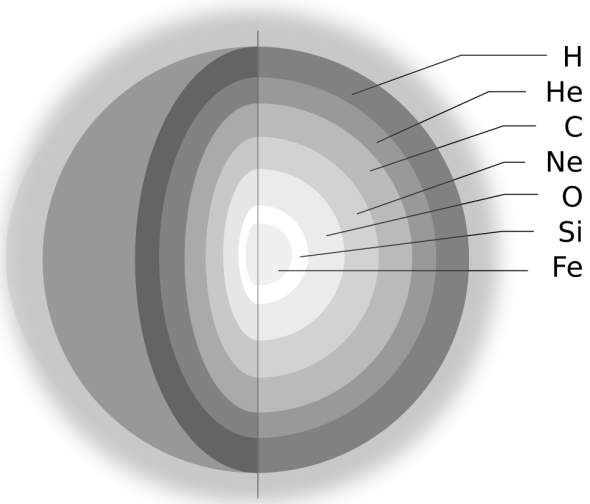

Figure 1.1: Example of onion-like structured star shells

via inverse β-decay releasing all the energy in a big burst. The collapse stops as neutrons start to degenerate and causing the implosion to rebound accelerating the remaining surrounding stellar material to escape velocity. The remnant degenerated core only consists of neutrons in a plasmic or solid state, a neutron star with a characteristic size of $R \approx 10\,\mathrm{km}$ and a mass between 1.44 and $3\,M_{\odot}$. Core masses above $3\,M\odot$ lead to the same supernova mechanism but leave a black hole instead of a NS.

The rapid decrease of the radius leads to extreme conditions. Because of angular momentum conservation the remnants have in general very short rotation periods (milliseconds up to a few seconds). Due to magnetic flux conservation during their birth, NS can have magnetic fields up to $10^{12}\,\mathrm{G}$.

These fast rotation of the magnetic field and the strong magnetic field in general interacts with surrounding matter and produces high energetic photons. In the case of XTE J1859+083 it is expected that the NS is in a binary system with a Be star.

The matter for the creation of the X-ray spectrum is supplied by the companion star and processed by the accretion of this matter onto the surface of the NS. Accretion is a very effective process to transform the energetic energy caused by the strong gravitational field into radiation energy. This matter can be transported either by a strong stellar wind or via the "Roche lobe overflow". In the latter case matter from the companion star exceeds the Roche lobe beyond the first Lagrangian point of the gravitational potential between both stars and is expected to happen in a high mass X-ray (HMXB) binary system, as XTE J1859+083 seems to be. A sketch of the matter transport by Roche lobe overflow is given in Fig. 1.2.

Due to the momentum conservation and other interactions the matter will form an accretion disk around the NS. This disk consists in general of plasma, gas and dust, while near the NS a plasma region is formed. The magnetic field forces the charged particles in the plasma to move in spirals around the field lines. Therefore near the surface matter can overall only follow parallel to the magnetic lines, forming a accretion column and hit the surface in the regions around the magnetic poles. Due to the circular motion of the charged particles the loss of kinetic energy is stored in radiation energy by cyclotron emission. In the outer parts of the accretion disk the hot matter deposits energy on photons via Compton scattering producing also X-ray photons in the surrounding of the NS.

From observations it is known that the accretion process in the column depends on the lu-

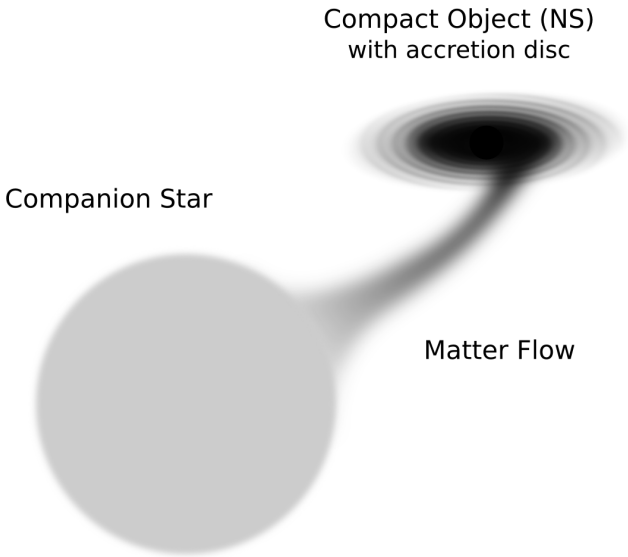

Figure 1.2: Sketch of a NS binary system

minosity of the matter near the surface. If the luminosity is below a critical luminosity L_c (depending on characteristic numbers of the NS, like the mass Becker et al., 2012) the plasma free falls onto the surface where photons get emitted perpendicular to it (Fig. 1.3(a)). If the luminosity exceeds L_c the emitted photons interact with the falling matter and decelerate them massively in a certain high above the surface over a short distance. This massive velocity change creates a shock front in the accretion column where after the plasma is no longer free falling (Fig. 1.3(b)) and photons leave the column sideways through the walls.

In the transition between $L \ll L_c$ and $L \gg L_c$ it is expected that a shock front is also created due to the pressure from the plasma. The remaining kinetic energy is then lost via coulomb breaking so the matter can rest at the stellar surface. The transition is continuous and leads to a mixture of all effects for $L \lesssim L_c$ (Becker et al., 2012). The case $L \ll L_c$ is expected for low mass X-ray binaries and $L \gg L_c$ for HMXB as XTE J1859+083.

In this thesis I will present the results achieved with the spectral model after Farinelli et al. (2012) on the observations of the outburst of XTE J1859+083. Further the analysis of the light curve and a new estimation for the of the source position.

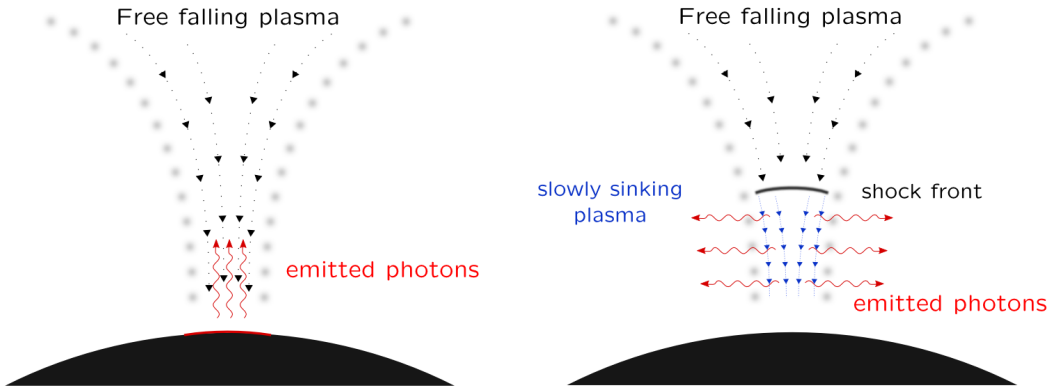

(a) Pencil beam (b) Fan beam

Figure 1.3: Sketch of the two accretion column types, according to Kretschmar (1996)

2 Technical Details

In this chapter I will give a short overview about the used instruments. Because most of the data analysis is done on the *NuSTAR* data this section will be more detailed than the one for *Swift*.

2.1 The Nuclear Spectroscopic Telescope Array (NuSTAR)

If not mentioned otherwise, this section is based on Harrison et al. (2013) The *NuSTAR* satellite is a 3 axis stabilized spacecraft launched mid 2012. With a very good resolution and sensitivity in the bandwidth of 3 – 79 keV *NuSTAR* provides detailed observations of X-ray sources in the high energy regime above 10 keV.

The observatory was launched into a 600 km, near-circular 6° inclined orbit to avoid most of the South Atlantic Anomaly (SAA). In principle it consists of 3 components, the optic modules, the focal plane and mast between those. The mast is deployed post-launch and extends the focal length to 10.14 m (see Fig. 2.1).

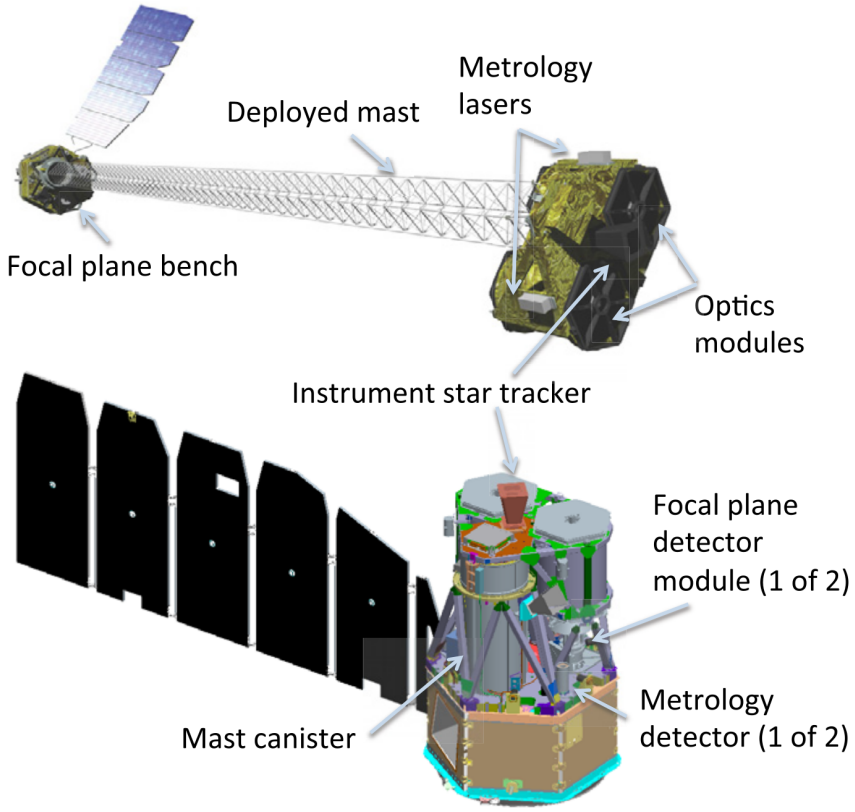

Figure 2.1: Diagram of the *NuSTAR* observatory in the stowed (bottom) and deployed (top) configurations (adopted from Harrison et al., 2013)

Table 2.1: The *NuSTAR* mission parameters

Mission Parameter	Value
Mass	350 kg
Power	600 W
Orbit	650 × 610 km
Orbit inclination	6°
Orbit lifetime	∼ 10 yr

Table 2.2: Key performance parameters of *NuSTAR*

Parameter	Value
Energy range	3 – 78.4 keV
Angular resolution (FWHM)	18″
Field of View (50% resp.) at 10 keV	10′
Field of View (50% resp.) at 68 keV	6′
Spectral resolution (FWHM)	400 eV at 10 keV, 900 eV at 68 keV
Strong source ($> 10\sigma$) positioning	$1.5''(1\sigma)$
Temporal resolution	2 µs

The *NuSTAR* optics module consist of two Wolter-I conical approximation optics which focus the X-rays onto two independent solid-state focal plane detectors, called fpmA and fpmB. To make it possible co-adding the images from both detectors, the optic's and detectors are designed to be as identical as possible. To determine the pointing direction and correlating accuracy the system is additionally equipped with a star camera mounted to the optics bench and two laser metrology units to measure the translation and other movement between the benches as well as the clocking. With the information from star camera and metrology system it is possible to reconstruct the instantaneous instrument alignment and pointing direction.

The angular resolution of the observatory is dominated by the optics, and is about 18″ at FWHM. Other key parameters are summarized in Table 2.1.

2.1.1 Optics

The *NuSTAR* optics modules are made of 133 nested multilayer-coated shells and arranged to build a conical approximation to the Wolter-I geometry. Each shell is built of 12 or 24 0.2 mm thin glass segments. The glass segments are coated with depth-graded multilayer structures (Pt/C at inner parts, W/Si at outer parts) to increases the graze angle above ∼ 15 keV. This results in a enhanced FoV at high energies. At the inner 89 shells the coating is made with depth graded Pt/C multilayers, reflect efficiently below the Pt K-absorption edge. The remaining layers are coated with depth-graded W/Si multilayers to reflect efficiently below the W K-absorption edge. For details about the manufacturing process of the optic modules (see, e.g., Koglin et al., 2005) and references therein. Because of the small grazing angle (angle between an on-axis incident X-ray and the optics shell) the effective FoV is limited to 10′ at 10 keV and 6′ at 68 keV. The optics angular response is dominated by structure errors in the substrates and of course by the mounting technique. But therefore *NuSTAR*s point spread function (PSF) is not a strong dependent on of off-axis angle. To first order the contour remains approximately constant with

Table 2.3: Focal plane parameters

Focal Plane Parameter	Value
Pixel size	$0.6\,\mathrm{mm}/12.3''$
Focal plane size	$12' \times 12'$
Hybrid format	$32\,\mathrm{pix} \times 32\,\mathrm{pix}$
Energy threshold	$2\,\mathrm{keV}$
Max. processing rate	$400\,\mathrm{evt\,s^{-1}\,module^{-1}}$
Max. flux meas. rate	$10^4\,\mathrm{cts\,s^{-1}}$
Time resolution (relative to on-board clock)	$2\,\mu\mathrm{s}$

off-axis angle.

2.1.2 Focal Plane

The module of each telescope consists of a solid state CdZnTe pixel detector placed in a CsI anti-coincidence shield. Each detector chip is made up of a two-by-two array of detectors, with a resolution of 32×32 pixels each. The detectors have an independent discriminators for each pixel and readout process is triggered by individual X-ray interactions. In this process the pixel row and column with the largest pulse height gets identified by the on-board processors, and they read out the information from this and eight neighbor pixels. The processing time ($2.5\,\mu\mathrm{s}$ per event) limits the rate for one chip to a number of 300 to 400 evt/s.

The processor from *NuSTAR* rejects events which deposit energy simultaneous in the detector and the anti-coincidence shield which results in an effective reduction of the background during the observation.

Characteristic numbers for the *NuSTAR* focal plane are given in Table 2.3.

2.1.3 Point Spread Function and Response

The PSF of *NuSTAR* is given in combination of the optics and the focal plane detector response combined with errors from the metrology system and the attitude reconstruction. Dominant contributors to the errors are the optics and of course the finite detector sampling. Bright source calibration measurements showed that the PSF for module B is within $2''$ of that of module A and the pointing direction is given with a $3''$ error radius.

Also from calibration measurements the soft X-ray regime normally agrees well with the measurements of other observatories. In the observation from XTE J1859+083 occurs a missmatch in the overlap between the "soft data" from *Swift* and the "hard data" from *NuSTAR*. Above 10 keV it is more difficult to compare the results because of the larger normalization factors and higher uncertainty. This will be discussed later, when combining the spectra extracted from *Swift* and *NuSTAR* data in chapter 4.

2.1.4 Data Analysis

The *NuSTAR* Analysis Software (NuSTARDAS) distributed as part of the HEASoft software package provided by the High Energy Archive Science Research Center (HEASARC) at NASA was used for data reprocessing and extraction. The software applies standard screening and calibration to the raw data. This includes, e.g., the correction for bad pixels, the metrology system and finally produces lightcurves spectra and images.

Table 2.4: *Swift*-XRT characteristics

Parameter	Value
Telescope	3.5 m focal length Wolter-I
Detector	e2v CCD-22
Detector size	600×600 pixels
Pixel size	$40\,\mu m/2.36''$
Field of View	$23.6'$
Time resolution	0.14 ms, 1.8 ms, 2.5 s
Energy range	0.2 – 10 keV
Sensitivity	$2 \cdot 10^{-14}$ erg cm^{-2} s^{-1} in 10^4 s

2.2 The Swift Gamma Ray Explorer

This section is mainly based on Burrows et al. (2005). A concise overview of the instruments on board the *Swift* satellite is also given by Krauß (2013). The *Swift* gamma ray explorer was mainly built to detect and observe gamma ray bursts (GRBs) and determine the position and redshift of the burst and the afterglow. Launched on 2004 November 20, the *Swift* satellite consists of three instruments: the Burst Alert Telescope (BAT) to identify GRBs and their location, the Ultraviolet/Optical Telescope (UVOT), and the essential X-ray Telescope (XRT).

2.2.1 XRT Optics and Detector

Similar to *NuSTAR* the *Swift* optics are built as a Wolter-I telescope to focus the X-rays on the CCD. The 600×600 pixels detector is thermoelectrically cooled to roughly -100 C. Each pixel has a size of $40\,\mu m \times 40\,\mu m$ and is sensitive to fluxes between 0.5 and 5 Crab in the 0.2 – 10 keV band.

The energy resolution for spectral analysis is about 140 eV at 6 keV. Timing resolution is between 0.14 ms and 2.5 s (depending on the readout mode). Other characteristics are shown in Table 2.4.

2.2.2 Data Analysis

Swift data is processed and provided by the Swift Data Center (SDC) at NASA. The analysis is done with the XRT Data Analysis Software (XRTDAS) consisting of FTOOL programs developed for the XRT instrument by ASI Science Data Center (ASDC) and HEASARC. The XRTDAS generates cleaned and corrected event files from the used instruments. The screening removes among others dead, hot and flickering pixels and transforms the raw data to sky and detector coordinates from the measured satellite attitude. The software supports the processing of all XRT readout modes.

For the spectral and lightcurve analysis the data of both observations from XTE J1859+083 are processed through the standard pipeline of the respective software packages. The observation parameters are given in Table A.3.

3 Source Position

The analysis of the picture allows to estimate the source position on the sky. For this source this is quite interesting because of the long quiescence phase. Therefore, the position is not very well known as well as the companion star can not get identified due to the high uncertainty on the source position.

To locate the source in the sky it is necessary to determine the maximal number of counts on the detector. Since *NuSTAR* has two detectors imaging the source, these have to be compared carefully. The *NuSTAR Performance Guide* (Harrison & Madsen (2009)) mentions that the point spread function (PSF) can be described as a KING profile

$$f_k(\boldsymbol{r}) = \left[1 + \frac{\boldsymbol{r}^2}{r_0^2}\right]^{-\alpha} \tag{3.1}$$

where r_0 denotes the width of the function and α describes the behavior of the wings. To fit the data points the KING profile is parametrized as

$$f_k(x, y) = \left[1 + \frac{(x - x_0)^2 + (y - y_0)^2}{r_0^2}\right]^{-\alpha}. \tag{3.2}$$

A much better result is achieved through an elliptical shape

$$\begin{aligned} f_k(x, y, \phi) = \Bigg[1 + \Bigg[\frac{(x - x_0) \cdot \cos(\phi) + (y - y_0) \cdot \sin(\phi)}{a}\Bigg]^2 + \\ + \Bigg[\frac{(y - y_0) \cdot \cos(\phi) - (x - x_0) \cdot \sin(\phi)}{b}\Bigg]^2\Bigg]^{-\alpha} \end{aligned} \tag{3.3}$$

where a and b are the semi major and minor axis and ϕ is the angle between the ellipse and the coordinate axis. The results of the position are shown in Table 3.1.

One can see that the estimated position differ slightly between the two chip modules. After Harrison et al. (2013) the PSF of both detectors are within $2''$ and the pointing accuracy of *NuSTAR* is $\pm 3''$. Since the calculated uncertainties are only from locating the maximum on the chip, one can see that they do not contribute to the $3''$ uncertainty of the metrology system. The position is then given by

$$\begin{aligned} \text{R.A.} &= 18^\text{h}\, 59^\text{m}\, 2.2^\text{s} \pm 0.2^\text{s} \\ \text{Dec} &= 8^\circ\, 14'\, 43'' \pm 3'' \end{aligned} \tag{3.4}$$

Table 3.1: Results of the KING profile fit and calculated sky position

			Detector Chip	
			Module A	Module B
Coordinates	Detector	x_0	499.986 ± 0.015	499.202 ± 0.015
		y_0	487.560 ± 0.014	487.505 ± 0.014
	Sky	R.A.	$18\text{h}\,59\text{m}\,2.2211\text{s} \pm 0.0025\text{s}$	$18\text{h}\,59\text{m}\,2.3509\text{s} \pm 0.0025\text{s}$
		Dec	$8^\circ\, 14'\, 43.10'' \pm 0.04''$	$8^\circ\, 14'\, 42.97'' \pm 0.04$

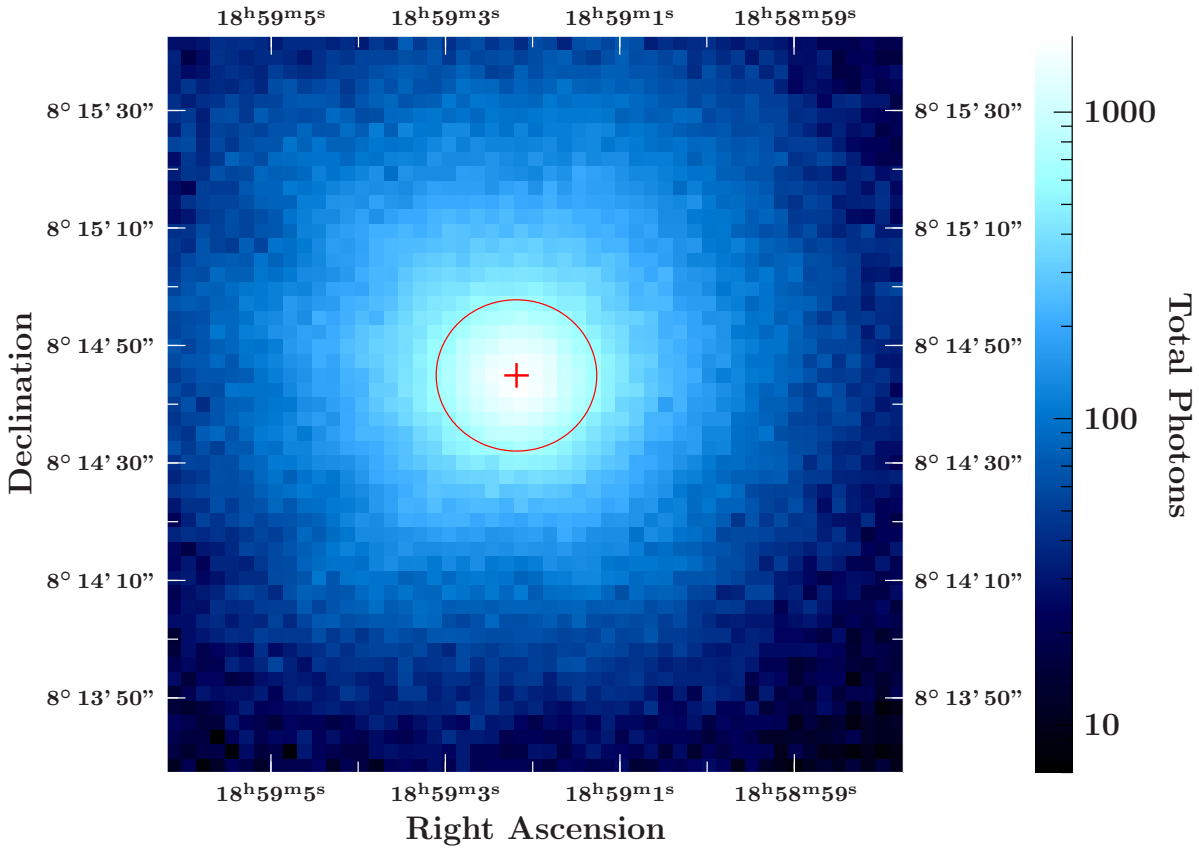

Figure 3.1: Section of detector module B. The red + indicates the estimated position for chip module B. The ellipse shows the elliptic shape of the fit.

and

$$\begin{aligned} \text{R.A.} &= 18^{\text{h}}\,59^{\text{m}}\,2.4^{\text{s}} \pm 0.2^{\text{s}} \\ \text{Dec} &= 8^{\circ}\,14'\,43'' \pm 3'' \end{aligned} \tag{3.5}$$

for chip A and B, respectively. The position of both detectors differ by little more then 2″ which is within the maximal expected uncertainty between both detectors. The errors on the estimated positions on the chip are very small. Contributors are underestimated errors from the image and also unhandled deviations from the approximation of the King profile. The main contribution to the errors on the pointing direction comes from the movement of the 10 m mast or rather the metrology system. Other contributors are thermal deformation and deviations in the structure. The image in Fig. 3.2 shows the calculated position in the *DSS2* sky image (red band). The dashed line indicates the error radius estimated by Corbet et al. (2009).

An alternative way to find the position of the source on the chip is to compare the observed image with archival PSF calibration images[1]. The problem here is finite resolution. Interpolating between the pixels may lead to similar values as calculated above.

To finally identify the optical counterpart of XTE J1859+083 it is encouraged to observe the estimated position in the UV since there are no observations done before. The continuum spectrum continues into the UV range so it should be possible to determine the system as a

[1]HEASARC calibration database (CALDB) http://heasarc.gsfc.nasa.gov/docs/heasarc/caldb/caldb_intro.html

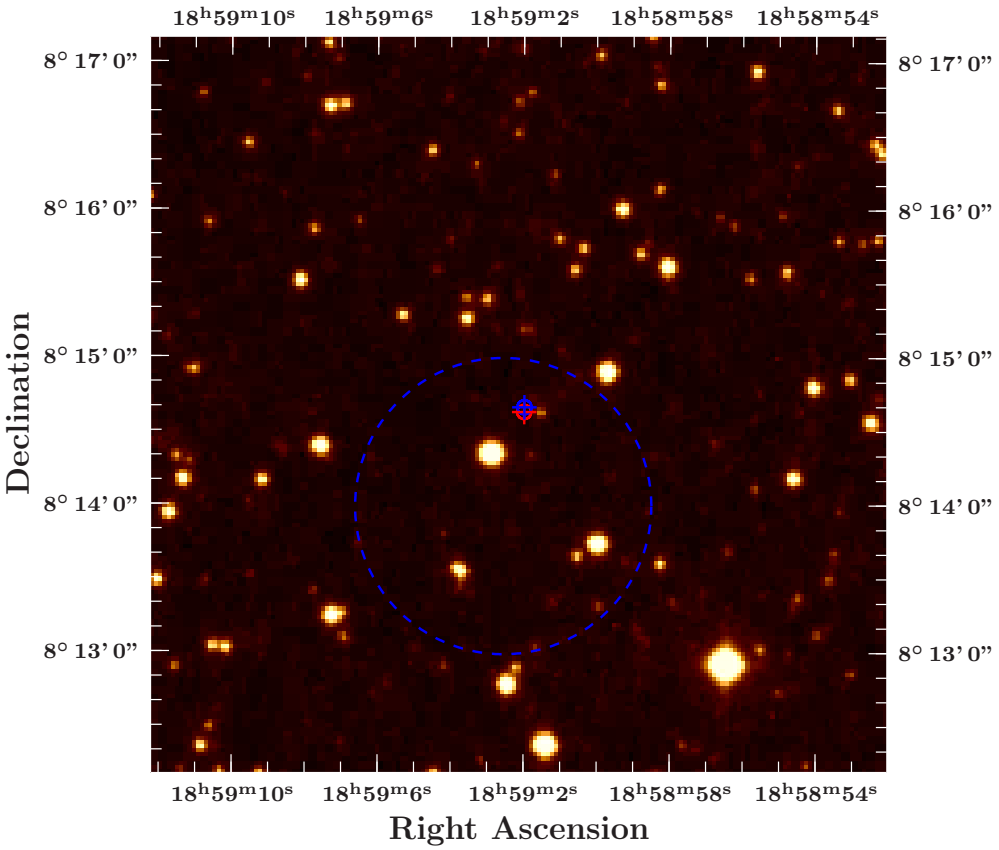

Figure 3.2: *DSS2* Image of the sky around the source. The blue +, red + displays the calculated source positions with error radius on chip module A and B, respectively. The dashed circle indicates the error radius after Corbet et al. (2009)

bright UV source. Hence, the companion star can be identified and will raise the understanding of the whole system.

4 Spectral Analysis

All data analysis in the next chapters is done with the Interactive Spectral Interpreting System (ISIS, Houck & Denicola 2000). The spectral data of both observations are described by one model in the 3 – 79 keV band. Because of some mismatch between the *NuSTAR* and *Swift* data in the soft X-rays as shown in Fig. 4.1, *NuSTAR* data below 5 keV was excluded for the simultaneous analysis. Furthermore one can see that the models and data disperse above 50 keV (e.g., 4.2). This may be caused by the large impact of the background there since it is nearly 1/3 of the signal. The data were binned such that the minimal signal to noise ratio is at least 20 over the complete bandwidth for *NuSTAR* and at least 10 for *Swift* in every bin.

The spectral analysis is somehow very difficult because the geometry and the processes around a neutron star are still not very good understood. In most cases the energy dependence can be described by a power law with an exponential cutoff. It should be obvious that a physical interpretation is mostly unreasonable because the connection between the fit parameters and physical properties is not easy to make. Nevertheless one can identify emission and absorption lines from the matter around the NS as well a cyclotron lines. These lines can be modeled via Gaussian or Lorentz profiles and the estimated energies indicate the atoms in the surrounding of the NS and in the companion star since for the emission lines only the participating atoms and their characteristic energy states are relevant[1].

Physical models, on the other hand, are very complicated but with the growing understanding of the accretion process in the past years more and more models try to describe the observed spectra under physical conditions. To apply the complex theoretical models to observed data

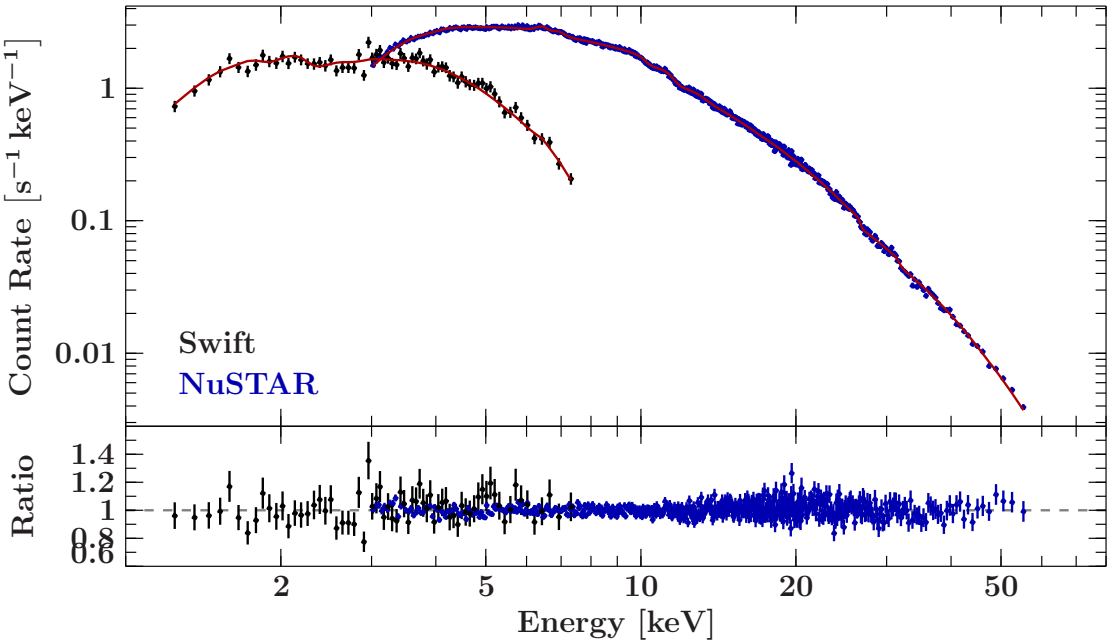

Figure 4.1: Concurrent fit through the full data from *Swift* and *NuSTAR*

[1] *NIST* X-ray transition energies database http://www.nist.gov/pml/data/xraytrans/index.cfm

in general one has to make assumptions for, e.g., the homogeneity of the temperature and the magnetic field in the accretion column. Many of these theories are only solvable under certain boundary conditions and it is of course topic today's debate whether this requirements are met or not. The general process producing X-ray spectra via accretion is the transformation from kinetic to radiation energy, but in detail one has to take care about many conditions around and inside the accretion column what can result in a long computation time of the models.

Observations could be first reproduced with a physical approach with more detailed knowledge about scattering features between high energetic photons and hot plasma. A huge step was done by consider not only Thomson scattering and comptonization but also differentiate between bulk and thermal comptonization (Becker & Wolff, 2007a). The new models then lead to the radiation process in the accretion columns. Due to the interaction between the infalling matter and the strong magnetic field lines the resulting spectrum is produced by cyclotron emission. But as already mentioned in chapter 1 the accretion close to the surface happens through the accretion column which is dependent on the luminosity and some critical luminosity (Becker et al., 2012). The different scenarios result in different X-ray spectra because of the difference between the "pencil beam" and "fan beam" case.

Here I used a exponential cutoff model for a general look at the spectra and the emission and absorption line identification. In the second part I applied the spectral model after Farinelli et al. (2012) to the data.

4.1 Exponential Cutoff Model

The power law cutoff model describes roughly the shape of X-ray spectra of accretion-powered X-ray pulsars. The model is described via

$$A_{\mathrm{cutoffpl}}(E) = K \cdot E^{-\gamma} \cdot \exp\left(-\frac{E}{E_{\mathrm{fold}}}\right) \tag{4.1}$$

where E is the corresponding energy, γ the power law photon index, E_{fold} the folding energy of exponential roll-off (in keV) and K the normalization. An additional black body spectrum B models the components in the soft X-ray. The absorption $A_{\mathrm{abs}}(E)$ of the X-rays in the interstellar medium was modelled with the `tbnew_simple` model[2] which is an updated version of the `tbabs` model. The cross sections and abundances for the absorption were set according to Verner et al. (1996) and Wilms et al. (2000), respectively. Additional Gaussian lines take the emission features of Iron in the accretion disk into account. The complete model then reads as

$$A(E) = A_{\mathrm{abs}}(E)\left(A_{\mathrm{cutoffpl}}(E) + G_1 + G_2 + G_3 + B\right). \tag{4.2}$$

The G_i are different Gauss profiles where G_1 and G_2 describe the K_α and K_β line of neutral iron. Because of the narrow lines the width were fixed to the lower limit of 10^{-6} keV. The K_β line was not significantly detected (lower panels in Fig. 4.2) but from our knowledge of atomic processes, K_β emission has to occur at a certain level in the presence of K_α emission. Furthermore, its inclusion does not introduce free model parameters since the line energy and flux of the K_β line can be constrained via the known relation between the energy level $E_{K_\alpha} - E_{K_\beta} = 0.656\,\mathrm{keV}$[3] and also the intensity $I_{K_\beta}/I_{K_\alpha} = 0.13$ (Hölzer et al., 1997).

In the ISIS routines (extended with the *isisscripts*[4]) the model is expressed as

```
tbnew_simple*(enflux(1,cutoffpl(1))+egauss(1)+egauss(2)+
egauss(3)+enflux(2,bbody(1)))
```

[2] http://pulsar.sternwarte.uni-erlangen.de/wilms/research/tbabs/

[3] *NIST* X-ray transition energies database http://www.nist.gov/pml/data/xraytrans/index.cfm

[4] *isisscripts* is a collection of ISIS scripts and functions provided by ECAP/Remeis observatory and MIT (http://www.sternwarte.uni-erlangen.de/isis/).

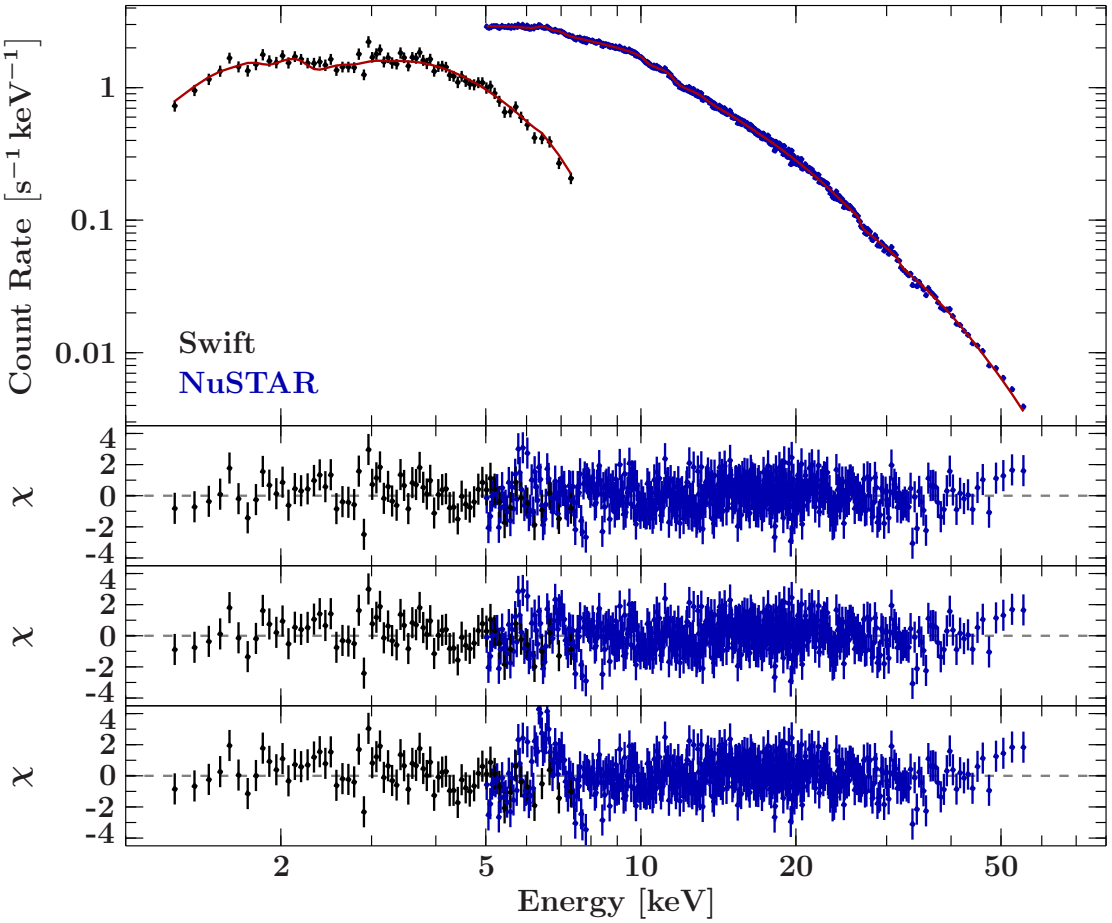

Figure 4.2: Non-physical exponential cutoff model with additional blackbody and Gauss peaks. The second and third residual panel show the fit without G_3 and no Gaussians, respectively. Data values are extracted from *NuSTAR* and *Swift* observations

where `enflux` converts the norm of the `cutoff` and `bbody` to a physical value. The parameters of the functions are referred to as `function.parameter`. As mentioned above *NuSTAR* data from 3 – 5 keV had to be excluded to avoid a mismatch between the *Swift* and *NuSTAR* spectrum during the fit. This mismatch is already known and will probably be resolved in future calibration updates.

One can see that the residuals are overall very flat, only a few emission lines can be seen between 6.4 keV and 7 keV. The two lower residual panels in Fig. 4.2 show how the fit behaves without G_3 and without any Gaussian. By consequently adding the Gaussians, the χ^2/d.o.f changes from 1246.423/1106 over 1141.689/1105 to 1123.015/1104. The final fit parameters for model are listed in Table 4.1.

Of interest are the parameters for the emission lines where the center parameter gives the maximum in keV and the norm (here the enflux parameter) of cutoff and bbody gives the photon counts in erg s^{-1} cm^{-2}. Overall the data from *NuSTAR* can be very well expressed with this model but some *Swift* data points do not fit perfectly probably due to noise and uncertainties in the instrument calibration.

The uncertainties are given at 90% confidence and calculated by varying the parameter of interest in small steps, refitting all other parameters to map the χ^2 landscape. As the best fit represents a (local) minimum, every deviation from it will increase the χ^2 and different confi-

Table 4.1: Summary of the variable parameters in the `cutoffpl + bbody` model

Parameter		Value
Absorption	`tbnew_simple.nH`	$(2.19 \pm 0.16) \cdot 10^{22}\,\mathrm{cm}^{-2}$
Cutoff Powerlaw	`cutoffpl(1).PhoIndex`	0.60 ± 0.05
	`cutoffpl(1).HighECut`	$16.4 \pm 0.6\,\mathrm{keV}$
	`enflux(1).enflux`	$(2.131 \pm 0.017) \cdot 10^{-9}\,\mathrm{erg\,s^{-1}\,cm^{-2}}$
Gauss 1	`egauss(1).area`	$(2.7 \pm 0.5) \cdot 10^{-4}\,\mathrm{photons\,s^{-1}\,cm^{-2}}$
	`egauss(1).center`	$6.44 \pm 0.05\,\mathrm{keV}$
Gauss 3	`egauss(3).area`	$(1.1 \pm 0.5) \cdot 10^{-4}\,\mathrm{photons\,s^{-1}\,cm^{-2}}$
	`egauss(3).center`	$6.88^{+0.12}_{-0.05}\,\mathrm{keV}$
Black Body	`bbody(1).kT`	$1.02 \pm 0.06\,\mathrm{keV}$
	`enflux(2).enflux`	$7.2^{+1}_{-0.9} \cdot 10^{-11}\,\mathrm{erg\,s^{-1}\,cm^{-2}}$

dence levels correspond to certain changes of chi^2. So here the parameters are assumed to be independent. If this is not the case the calculated error values are wrong and how much they differ from the real value depends directly on the correlation between the parameters.

4.2 Model after Farinelli et al. (2012)

The model developed by Farinelli et al. (2012) is a numerical solution of the radiative transfer equation (RTE) and is implemented in the ISIS software package as `compmag` model. The RTE describes the energy transfer from electromagnetic waves through an optical medium where the wave is affected by emission, absorption and scattering. Analytic solutions are only possible under unrealistic assumptions, for more physical situations only numeric solutions are possible. Even the numerical treatment of the problem requires some simplifying assumptions such as a cylindrical symmetry of the accretion column. Farinelli et al. (2012) assumed that the photon energy exchange for scattering is low ($\Delta\nu/\nu \ll 1$) so it is possible to do a Taylor expansion of the Comptonization operator, which transforms the RTE from integro-differential (Pomraning, 1973) to purely differential (Rybicki & Lightman, 1985). This is known as the Fokker-Planck approximation. This approach is only justified if the electron temperature kT_e is subrelativistic ($\lesssim 100\,\mathrm{keV}$).

After all the solution of the RTE is found in an iterative process by solving an elliptic partial differential equation with given boundary conditions. The algorithm finally finds the approximated solution via a relaxation method. The algorithm stops when the spectral index of the powerlaw regime of the iterated solution fulfills some convergence criterion. This criterion ensures also that the norm of the solution converged.

For the algorithm it is necessary to define the behaviour of the velocity profile $\beta(\tau)$ in the column as a function of the optical depth. In the `compmag` model the user can choose between two velocity profiles (eq. 4.3 and eq. 4.4 Farinelli et al., 2012). The second velocity was proposed by Becker & Wolff (2007b).

$$\beta(\tau) = -\mathrm{A}\left\{ z_0^{\eta+1} + \frac{\mathrm{A} r_0^2 (1+\eta)\tau}{2.2 \cdot 10^{-3} \dot{m}} \right\}^{-\frac{\eta}{\eta+1}} \tag{4.3}$$

$$\beta(\tau) = -\Psi\tau \tag{4.4}$$

where A is a defined normalization constant (terminal velocity at given altitude), z_0 the vertical coordinate at the NS surface, r_0 the radius of the accretion column, η the index of the velocity

Table 4.2: Summary of the variable fit parameters in `compmag`

Parameter	Units	Description
kT_{bb}	(keV)	Seed photon blackbody temperature
kT_{e}	(keV)	Electron temperature
τ		Optical depth of the accretion column
η		Index of the velocity profile
β_0		Terminal velocity at the NS surface
r_0		Radius of the accretion column in units of the NS Schwarzschild radius
A		Albedo at the NS surface
Flag		$= 1$, $\beta(\tau)$ from eq. 4.3 $= 2$, $\beta(\tau)$ from eq. 4.4
Norm		$R^2_{\mathrm{km}}/D^2_{10}$, R_{km} BB emitting area in km and D_{10} source distance in 10 kpc

Table 4.3: Resulting parameters for `compmag` with $\beta(\tau)$ from eq. 4.4

Parameter		Value
Absorbtion	`tbnew_simple(1).nH`	$\left(2.41^{+0.31}_{-0.22}\right) \cdot 10^{22}\,\mathrm{cm}^{-2}$
Compmag	`compmag(1).kTbb`	$0.69^{+0.07}_{-0.09}\,\mathrm{keV}$
	`compmag(1).kTe`	$5.27^{+0.17}_{-0.22}\,\mathrm{keV}$
	`compmag(1).tau`	$0.584^{+0.008}_{-0.028}$
	`compmag(1).r0`	$0.5877^{+0.0012}_{-0.0570}$
	`compmag(1).A`	$0.638^{+0.249}_{-0.024}$
	`enflux(1).enflux`	$2.201^{+0.012}_{-0.009} \cdot 10^{-9}\,\mathrm{erg\,s^{-1}\,cm^{-2}}$
Gauss 1	`egauss(1).area`	$(2.7 \pm 0.5) \cdot 10^{-4}\,\mathrm{photons\,s^{-1}\,cm^{-2}}$
	`egauss(1).center`	$6.422^{+0.056}_{-0.024}\,\mathrm{keV}$
Gauss 3	`egauss(3).area`	$(1.1 \pm 0.4) \cdot 10^{-4}\,\mathrm{photons\,s^{-1}\,cm^{-2}}$
	`egauss(3).center`	$6.84^{+0.11}_{-0.09}\,\mathrm{keV}$

profile and $\dot{m}$ the mass accretion in Eddington units and $\Psi = 0.67\zeta/z_0$ with $\zeta = \frac{15.8 r_0}{\dot{m}}$. All variable fit parameters are given in Table 4.2.

The compmag model is a pure continuum model and modified by additional Gaussian lines and the ISM absorption similar to the cutoff model.

```
tbnew_simple(1)*(enflux(1, compmag(1))+egauss(1)+egauss(2)+egauss(3))
```

The linear velocity profile is indeed easier to handle for several fit algorithms but the result is very good (Fig. 4.3) and the best fit parameters are given in Table 4.3.

For the velocity profile given in eq. 4.3 the χ^2 of the model seems to have many local minima where the fit stops. Using more advanced fit algorithms to find the global minimum tends to fail during the runtime. The best fit parameters are summarized in Table 4.4 and Fig. 4.4 shows the corresponding plot. One can see that the change in the velocity profile leads to similar results for the other model parameter.

Believing the resulting parameters, the observed source is a compact object with Albedo similar to the Venus, therefore roughly 64% of infalling light will be reflected from the surface. Since

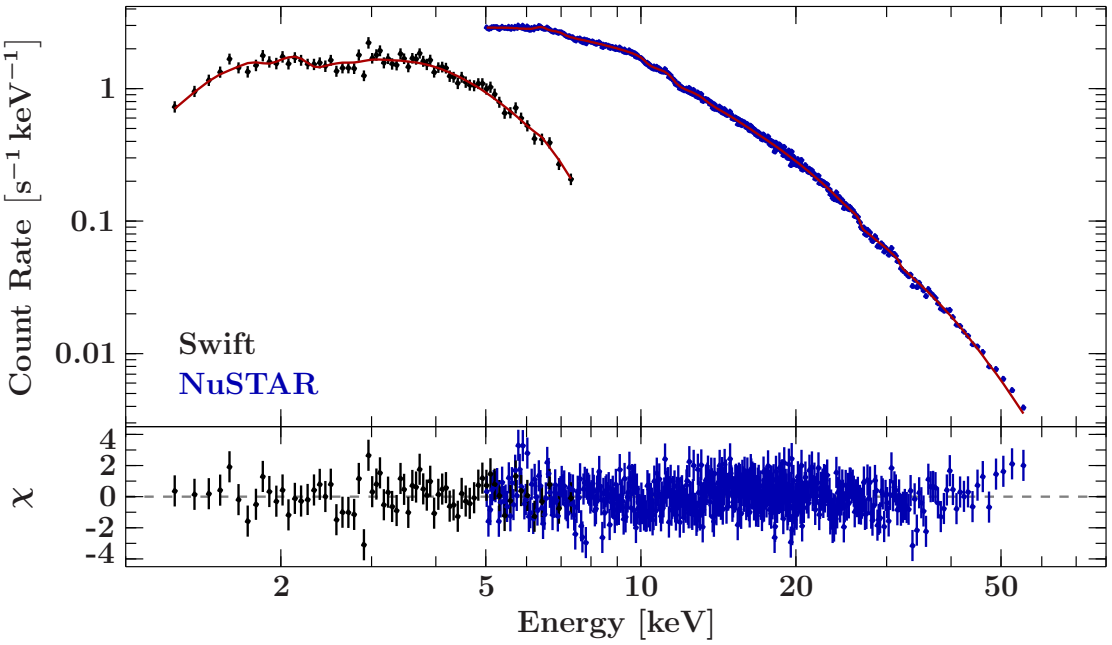

Figure 4.3: Physical model after Farinelli et al. (2012) with additional Gaussians over the phase averaged spectrum. Velocity profile from eq. 4.4. Data values are extracted from *NuSTAR* and *Swift* observations

the radius of the accretion column is only given in units of the source Schwarzschild radius and an object with a mass $M = 2\,M_\odot$ and a radius of $r = 10\,\mathrm{km}$ (which is common for NS) has a Schwarzschild radius of roughly 6 km and so the accretion column covers nearly 3% of the surface (in case of two columns obviously 6%). Compared to the cutoff model the energy of the blackbody spectrum is very similar in both models, what is indeed surprising since the degrees of freedom for the blackbody are in the cutoff model 2 and in compmag only 1. The corresponding temperature for the blackbody and electron gas is $T_{\mathrm{bb}} \approx 1.2 \cdot 10^7\,\mathrm{K}$ and $T_{\mathrm{e}} \approx 5.8 \cdot 10^7\,\mathrm{K}$, respectively. For the optical depth of the accretion disk only an upper limit can be derived to $\tau \leq 0.8$.

4.3 Phase resolved Spectra

To understand the process of the accretion even further and get an idea about the geometry of the system it is useful to analyze the spectrum from in different states of the rotation phase. The extracted spectra from from segments of the rotation period show the NS under different angles. This can be used to take a look on the geometry of the accretion column and disk. I extracted spectra in evenly spaced intervals only taking the counts in the belonging phase interval into account. The explicit phase cuts are shown in the phase profile in Fig. 5.1.

Since the lightcurve analysis is only done on the *NuSTAR* data, I used the full bandwidth for the phase resolved spectra analysis. To see how the spectrum changes with the rotation phase the resulting fit functions from the models after Farinelli et al. (2012) with both velocity profiles are shown in Fig. 4.5 and 4.6.

One can see that the intensity varies over the phase in the expected way since the photon emitting region is only partial in the line of sight. The modeled spectra fit very well to the phase resolved data (Table **??** shows the belonging chi^2 statistics). In Fig. 4.6 the difference between the phase resolved and phase averaged spectra span a wider range then in Fig. 4.5. The phase averaged spectra best fit parameters are given in Table A.1 and A.2 and displayed in Fig. A.1.

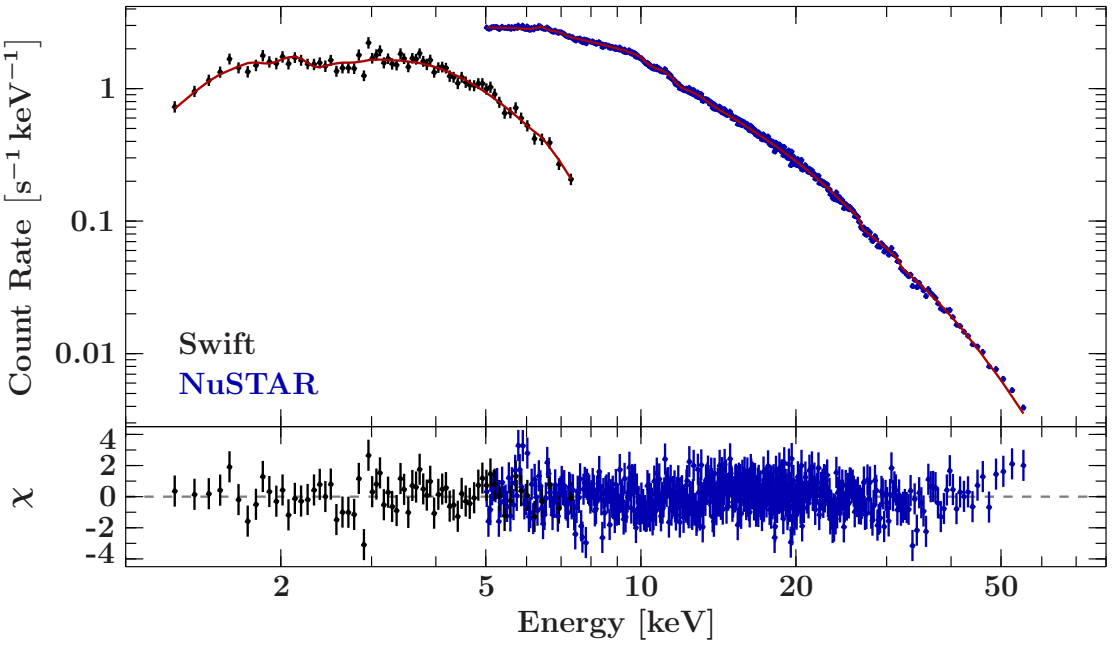

Figure 4.4: Physical model after Farinelli et al. (2012) with additional Gaussians over the phase averaged spectrum. Velocity profile from eq. 4.3. Data values are extracted from *NuSTAR* and *Swift* observations

Table 4.4: Resulting parameters for `compmag` with $\beta(\tau)$ from eq. 4.3

Parameter		Value
Absorbtion	`tbnew_simple(1).nH`	$2.41^{+0.09}_{-0.08} \cdot 10^{22}\,\mathrm{cm}^{-2}$
Compmag	`compmag(1).kTbb`	$0.692^{+0.025}_{-0.036}\,\mathrm{keV}$
	`compmag(1).kTe`	$5.273^{+0.201}_{-0.006}\,\mathrm{keV}$
	`compmag(1).tau`	$0.584^{+0.007}_{-0.004}$
	`compmag(1).r0`	$0.588^{+0.019}_{-0.011}$
	`compmag(1).A`	$0.6377^{+0.0022}_{-0.0208}$
	`compmag(1).eta`	≤ 0.8
	`compmag(1).beta0`	$0.0435^{+0.4924}_{-0.0013}$
	`enflux(1).enflux`	$2.201^{+0.007}_{-0.005} \cdot 10^{-9}\,\mathrm{erg\,s}^{-1}\,\mathrm{cm}^{-2}$
Gauss 1	`egauss(1).area`	$(2.7 \pm 0.4) \cdot 10^{-4}\,\mathrm{photons\,s}^{-1}\,\mathrm{cm}^{-2}$
	`egauss(1).center`	$6.421^{+0.044}_{-0.023}\,\mathrm{keV}$
Gauss 3	`egauss(3).area`	$\left(1.05^{+0.09}_{-0.36}\right) \cdot 10^{-4}\,\mathrm{photons\,s}^{-1}\,\mathrm{cm}^{-2}$
	`egauss(3).center`	$6.84^{+0.12}_{-0.09}\,\mathrm{keV}$

The variation in the iron emission lines is maybe only due to the lower count rate and so they are just not significantly detected.

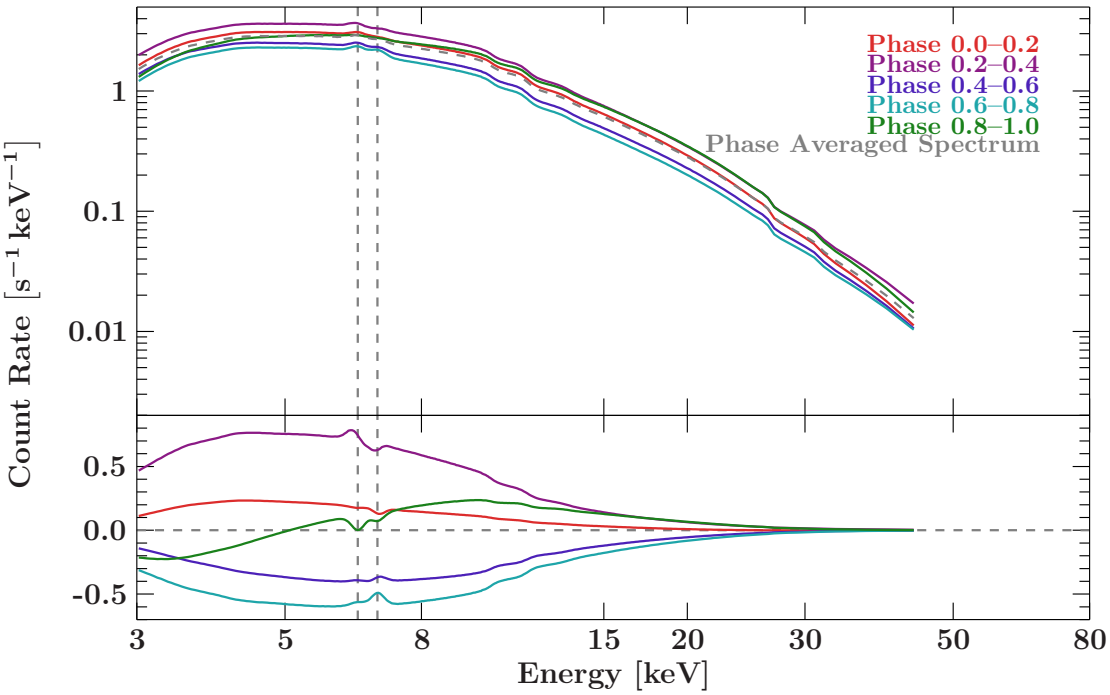

Figure 4.5: Phase resolved spectra fitted with `compmag`, $\beta(\tau)$ from eq. 4.4. Grey dashed vertical lines indicate estimated iron emission features. Lower panel shows the individual difference between phase resolved and phase averaged spectra.

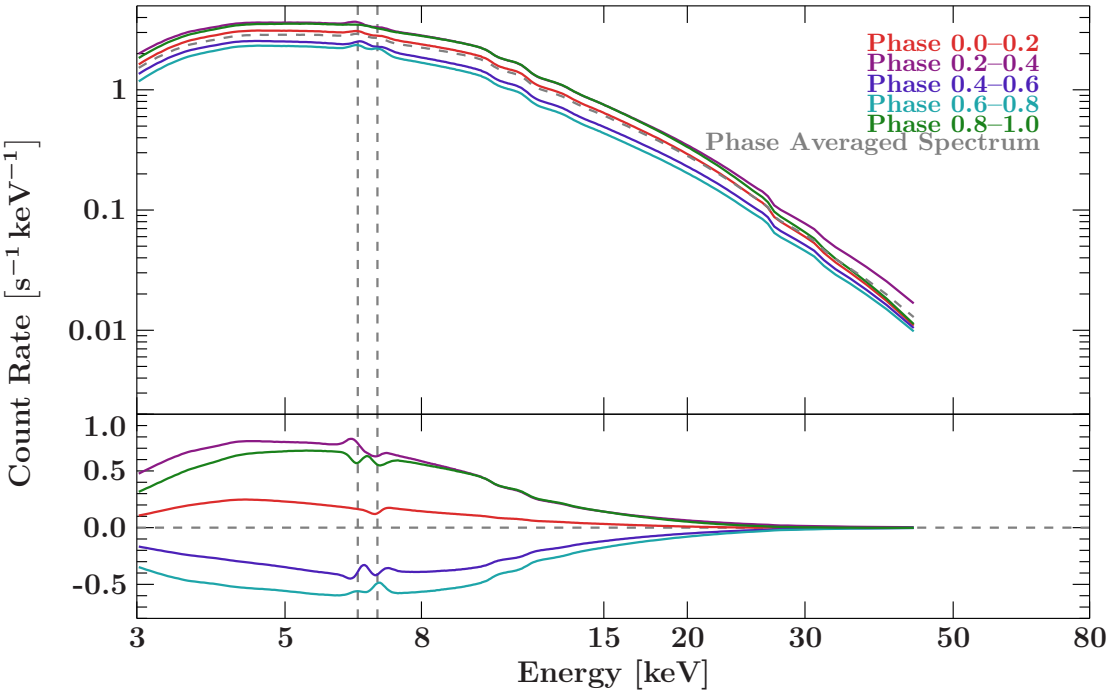

Figure 4.6: Phase resolved spectra fitted with `compmag`, $\beta(\tau)$ from eq. 4.3. Grey dashed vertical lines indicate calculated iron emission features. Lower panel shows the individual difference between phase resolved and phase averaged spectra

5 Pulse Profile

The mass accretion rate onto the surface of the NS is not independent off the rotation period because the matter must rotate with the same angular velocity around the NS to come to rest at its surface. A variable rotation period results in a variable accretion rate. Furthermore the accretion geometry is dependent on the period which makes it necessary to examine the rotation period P of the NS.

Since a high amount of photons gets emitted around the magnetic pole regions, the observed lightcurve shows a periodical behavior, increase or decrease when pole regions come in line of sight or leave. From this one can calculate the pulse period either via Fourier transformation or epoch folding (Leahy et al., 1983; Kühnel, 2011).

For the analysis here I used the epoch folding method, which will briefly discussed here. The idea is to fold the data on a assumed test period P_t, distribute the events in phase bins and calculate a histogram from the event distribution. If $P_t = P$ the histogram represents the pulse profile of the source, which is the measured photon count rate at different phase bins. To distribute the events one has to convert the time into pulse phase via

$$\phi = \frac{t \bmod P_t}{P_t}. \tag{5.1}$$

The histogram for a count rate I is then calculated for a given number of phase bins n by

$$H_i = \frac{P_t}{T} \sum I(i/n \leq \phi < (i+1)/n) \tag{5.2}$$

where i is the index of the phase bin and T the length of the extracted lightcurve. H_i is then the mean count rate per phase bin i. In the case that $P_t \neq P$ the periodicity vanishes on average with increasing difference between P_t and P.

To calculate the real period one can apply χ^2-statistics between the averaged count rate in one bin I_i and the mean count rate of the pulse profile $\langle I \rangle$.

$$\chi^2 = \sum_{i=1}^{n} \frac{(I_i - \langle I \rangle)^2}{\sigma_i^2} \tag{5.3}$$

where $\sigma_i^2 = \langle I \rangle / T_i$ with T_i the integration time for bin i. It is not hard to see that the maximum value for χ^2 is achieved when $P_t = P$ then of course the profile is not constant.

With epoch folding calculated periods are obviously afflicted by uncertainties because the observation time for the lightcurve is finite. The shorter the observation time is, the more is the peak around the real period broadened and side maxima occur. Things get worse when the signal to noise ratio is low. With a clear pulsation signal and a high signal to noise ratio the pulsation period distribution looks like a Gaussien distribution (besides the side maxima) but only if the variability of the period is small in the observed lightcurve.

A rough error estimation is given by the difference between two statistical independent periods P and P'. One can calculate this from the change of the pulse period in a lightcurve of lenght T with number of pulsations n and $n+1$

$$\Delta P = |P - P'| = \frac{T}{n} - \frac{T}{n+1} \tag{5.4}$$

The number of pulsations is approximately given by $n \approx \frac{T}{P}$, inserting this and neglecting the 1 for long observations, leads to

$$\Delta P \approx \frac{P^2}{T}. \tag{5.5}$$

This shows that the accuracy only depends on the observation time of the lightcurve. For complex profiles and a better results the uncertainty gets calculated with Monte Carlo simulations. These simulations create lightcurves based on the calculated pulse profile and randomize them according to the measured noise. Individually creating pulse profiles from these simulated lightcurves via epoch folding leads to normal distributed pulse periods around the initially calculated period. The uncertainty of the period is then given by the according standard deviation.

With epoch folding and Monte Carlo simulations the calculated rotation period of XTE J1859+083, based on the *NuSTAR* lightcurve is $P = 9.791507 \pm 8 \cdot 10^{-6}$ s. This is in accordance to Corbet et al. (2009) and accommodating for XTE J1859+083 being a Be/NS binary.

In Fig. 5.1 the related pulse profile is shown for the full energy spectrum (bottom panel). It is often observed that NS binaries show a high variability in the pulse profile in different energy ranges. For the outburst of XTE J1859+083 it is very suspicious that the pulsation is nearly the same in every energy range. Also very surprising is the fact that the pulsation is very symmetrical, a longer pulse ($t \approx 0.4 \cdot P$) followed by a short one ($t \approx 0.1 \cdot P$) of nearly the same intensity in all energy ranges. Only the second pulse in the soft X-ray 3 –5 keV band is significant smaller then the first one. The oscillation in the higher ranges can be explained with the low rate of photon events in this energy range. The calculated profiles in the high energy regimes probably does not reproduce the real pulsation because high photon events are rare as it can be seen in the spectra in chapter 4.

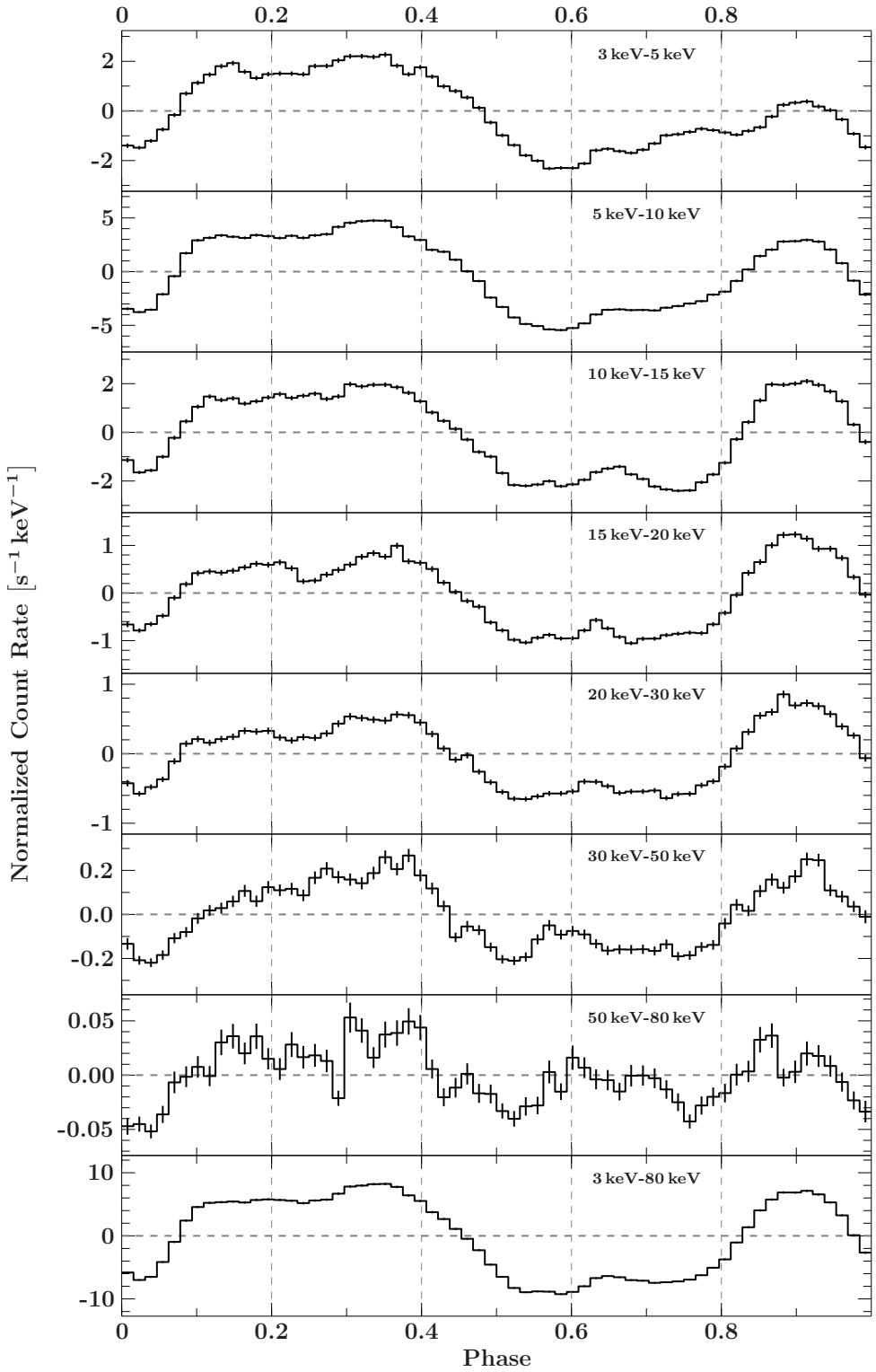

Figure 5.1: The pulse profile of the source in different energy ranges. The gray dashed vertical lines indicate different phase intervals used in the spectral analysis

6 Conclusion

The outburst from XTE J1859+083 early 2015 can be very good modeled with the spectral model reported from Farinelli et al. (2012). The approach with the compmag model shows no significant difference to the often used exponential cutoff model. Therefore compmag might be a good physical approach for many X-ray sources if some minor problems in the algorithm can be fixed.

Further, XTE J1859+083 exhibits two significant iron emission features. The known transition of the K_α level and another certainly ionized iron transition at 6.84 keV.

In accordance to Marshall et al. (1999) the rotation period of the NS is 9.8 s and seems not to be variable in timescales of years. In different energy ranges XTE J1859+083 shows no variation in the pulse profile.

The attempt to locate the source with a lower uncertainty showed that the accuracy is highly dominated by the pointing accuracy of the *NuSTAR* satellite, the detector chips only add uncertainties orders of magnitudes smaller then the one from the metrology system. Only when combining both detector images they show uncertainties in the same order as the metrology system.

Acknowledgments

I would like to extend thanks to everyone supported me during the work for this thesis. Special thanks go to Jörn Wilms for introducing me to the X-ray field and the opportunity to write this thesis at the Remseis observatory in Bamberg. Further, I would like to thank Matthias Kühnel and Christoph Großberger for support on the technical side and showing me some programming tricks. Very special thanks go to Ralph Ballhausen who helped me to get hands on scientific X-ray data, proofread my thesis many times and never got tired answering my questions even during his final phase of his master's thesis.

I would like to thank everyone at the Remeis observatory for a very instructive and nevertheless friendly and collegial atmosphere.

References

Becker, P. A., Klochkov, D., Schönherr, G., et al. 2012, A&A, 544, A123

Becker, P. A. & Wolff, M. T. 2007a, ApJ, 654, 435

Becker, P. A. & Wolff, M. T. 2007b, ApJ, 654, 435

Burrows, D. N., Hill, J. E., Nousek, J. A., et al. 2005, SSR, 120, 165

Corbet, R. H. D., in't Zand, J. J. M., Levine, A. M., & Marshall, F. E. 2009, ApJ, 695, 30

Farinelli, R., Ceccobello, C., Romano, P., & Titarchuk, L. 2012, A&A, 538, A67

Harrison, F. & Madsen, K. 2009

Harrison, F. A., Craig, W. W., Christensen, F. E., et al. 2013, ApJ, 770, 103

Houck, J. C. & Denicola, L. A. 2000, in Astronomical Society of the Pacific Conference Series, Vol. 216, Astronomical Data Analysis Software and Systems IX, ed. N. Manset, C. Veillet, & D. Crabtree, 591

Hölzer, G., Fritsch, M., Deutsch, M., Härtwig, J., & Förster, E. 1997, Phys. Rev. A, 56, 4554

Koglin, J. E., Christensen, F. E., Craig, W. W., et al. 2005, in Proc. SPIE, Vol. 5900, Optics for EUV, X-Ray, and Gamma-Ray Astronomy II

Krauß, F. 2013, Master's thesis, Friedrich-Alexander-Universität Erlangen-Nürnberg

Kretschmar, P. 1996, Dissertation, Eberhard-Karls-Universität zu Tübingen

Krimm, H. A., Barthelmy, S. D., Baumgartner, W., et al. 2015, The Astronomer's Telegram, 7037, 1

Kühnel, M. 2011, Master's thesis, Friedrich-Alexander-Universität Erlangen-Nürnberg

Leahy, D. A., Darbro, W., Elsner, R. F., et al. 1983, ApJ, 266, 160

Marshall, F. E., in 't Zand, J. J. M., Strohmayer, T., & Markwardt, C. B. 1999, IAUC, 7240, 2

Negoro, H., Suzuki, K., Namba, T., et al. 2015, The Astronomer's Telegram, 7034, 1

Pomraning, G. C. 1973, The equations of radiation hydrodynamics (Pergamon Press)

Romano, P., Sidoli, L., Mangano, V., & Mereghetti, S. 2007, The Astronomer's Telegram, 1287, 1

Rybicki, G. B. & Lightman, A. P. 1985, Radiative Processes in Astrophysics (Wiley)

Smartt, S. J. 2009, ARAA, 47, 63

Verner, D. A., Ferland, G. J., Korista, K. T., & Yakovlev, D. G. 1996, ApJ, 465, 487

Wilms, J., Allen, A., & McCray, R. 2000, ApJ, 542, 914

A Appendix

Table A.1: Resulting parameters for `compmag` (only *NuSTAR*, $\beta(\tau)$ from eq. 4.4)

	Parameter	Value
Absorbtion	`tbnew_simple(1).nH`	$2.87 \pm 0.23 \cdot 10^{22}\,\mathrm{cm}^{-2}$
Compmag	`compmag(1).kTbb`	$0.36 \pm 0.12\,\mathrm{keV}$
	`compmag(1).kTe`	$5.3^{+0.6}_{-0.4}\,\mathrm{keV}$
	`compmag(1).tau`	$0.62^{+0.12}_{-0.08}$
	`compmag(1).r0`	$0.60^{+0.09}_{-0.05}$
	`compmag(1).A`	$0.40^{+0.11}_{-0.15}$
	`enflux(1).enflux`	$2.326 \pm 0.012\,\mathrm{erg\,s}^{-1}\,\mathrm{cm}^{-2}$
Gauss 1	`egauss(1).area`	$(2.9 \pm 0.5) \cdot 10^{-4}\,\mathrm{photons\,s}^{-1}\,\mathrm{cm}^{-2}$
	`egauss(1).center`	$6.404^{+0.054}_{-0.006}\,\mathrm{keV}$
Gauss 3	`egauss(3).area`	$(1.1 \pm 0.4) \cdot 10^{-4}\,\mathrm{photons\,s}^{-1}\,\mathrm{cm}^{-2}$
	`egauss(3).center`	$6.88^{+0.09}_{-0.12}\,\mathrm{keV}$

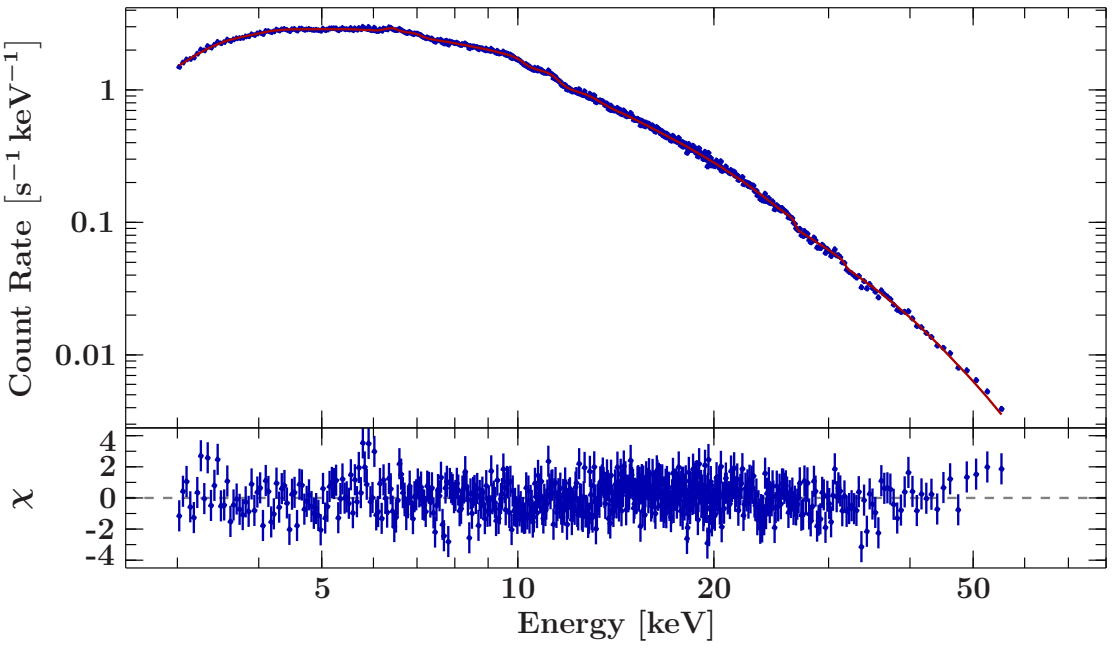

(a) $\beta(\tau)$ from eq. 4.4

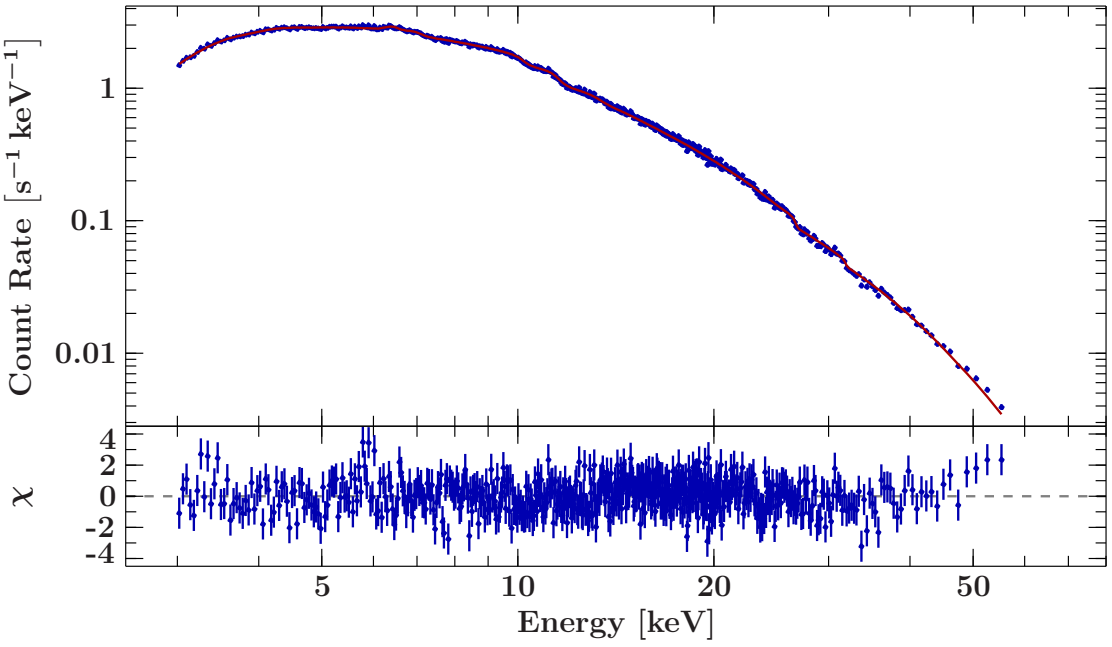

(b) $\beta(\tau)$ from eq. 4.3

Figure A.1: Best compmag fit to *NuSTAR* spectrum

Table A.2: Resulting parameters for `compmag` (only *NuSTAR* $\beta(\tau)$ from eq. 4.3)

Parameter		Value
Absorbtion	`tbnew_simple(1).nH`	$3.37^{+0.08}_{-0.35} \cdot 10^{22}\,\mathrm{cm}^{-2}$
Compmag	`compmag(1).kTbb`	$0.39^{+0.06}_{-0.12}\,\mathrm{keV}$
	`compmag(1).kTe`	$4.7412^{+0.0014}_{-0.0155}\,\mathrm{keV}$
	`compmag(1).tau`	$0.5201^{+0.0009}_{-0.0266}$
	`compmag(1).r0`	≤ 0.5
	`compmag(1).A`	$0.8740^{+0.0006}_{-0.3785}$
	`compmag(1).eta`	≤ 0.4
	`compmag(1).beta0`	$0.1762^{+0.0004}_{-0.0166}$
	`enflux(1).enflux`	$(2.334^{+0.004}_{-0.011}) \cdot 10^{-9}\,\mathrm{erg\,s^{-1}\,cm^{-2}}$
Gauss 1	`egauss(1).area`	$\left(2.9^{+0.5}_{-0.4}\right) \cdot 10^{-4}\,\mathrm{photons\,s^{-1}\,cm^{-2}}$
	`egauss(1).center`	$6.413^{+0.052}_{-0.014}\,\mathrm{keV}$
Gauss 3	`egauss(3).area`	$\left(1.08^{+0.38}_{-0.06}\right) \cdot 10^{-4}\,\mathrm{photons\,s^{-1}\,cm^{-2}}$
	`egauss(3).center`	$6.879^{+0.008}_{-0.060}\,\mathrm{keV}$

Table A.3: Observation parameters from XTE J1859+083 on March 3rd 2015

Satellite	R.A.	Dec	Time	Obs ID	Exposure Time
NuSTAR	18:59:06.8	+08:16:27	2015-03-30 17:16:07	90001010002	19839 s
Swift	18:59:12.47	+08:14:40.6	2015-03-30 22:05:59	00037043011	1154.46400 s (XRT)

Table A.4: χ^2 statistics for phase resolved spectra fits

		$\beta(\tau)$ from eq. 4.3	$\beta(\tau)$ from eq. 4.4
χ^2/d.o.f.	phase 0 – 0.2	641.4876/636	639.7053/638
	phase 0.2 – 0.4	775.9357/684	771.2065/686
	phase 0.4 – 0.6	604.1135/568	597.5703/570
	phase 0.6 – 0.8	578.7597/544	567.3712/546
	phase 0.8 – 1	714.0664/678	723.7365/670

List of Figures

List of Tables

Erklärung

Hiermit bestätige ich, dass ich diese Arbeit selbstständig und nur unter Verwendung der angegebenen Hilfsmittel angefertigt habe.

Bamberg, 30. November 2015
Ort, Datum

Jakob Stierhof